Computational Materials Science 184 (2020) 109897

Contents lists available at ScienceDirect

Computational Materials Science

journal homepage: www.elsevier.com/locate/commatsci

First-principles calculations on high-temperature desorption loss from iridium

Insung Seo[a], Shunsuke Yokota[b], Yousuke Imai[b], Yoshihiro Gohda[a,*]

[a] Department of Materials Science and Engineering, Tokyo Institute of Technology, Yokohama 226-8502, Japan
[b] ISHIFUKU Metal Industry Co., Ltd., Soka 340-0002, Japan

ARTICLE INFO

Keywords:
First-principles calculations
Surface
Thermodynamics
Volatile oxide
Desorption

ABSTRACT

We examine the IrO_3 desorption from iridium surfaces using first-principles calculations. To investigate out-of-equilibrium adsorption–desorption steps, we estimate the temperature dependence of changes in the free energy considering molecular excitation. Our result shows that the IrO_3 desorption occurs at a specific temperature range. In addition to kinks, we identify that the terrace of the Ir(111) surface is active for the IrO_3 desorption in contrast to the less-close-packed (100) and (110) surfaces. The absence of a transition state is found during the desorption process.

1. Introduction

Oxidation loss at high temperatures is mainly caused by the formation of volatile oxides that is universally seen for transition metals [1]. This is well recognized for molybdenum as one of the challenging issues for its lifetime, where oxidation of Mo results in desorption of MoO_3 above around 550 K [2]. In addition, the formation of gaseous oxides is also problematic for iridium because of its usage at high temperatures: Iridium is typically used as spark plugs of internal combustion engines and crucibles for the single crystal growth due to the remarkable mechanical strength and chemical inertness. [3–6]. It has been reported that volatile oxides are formed above 1373 K [7], and, thus, desorption behaviors of iridium as gaseous oxides have attracted much attention. Even though IrO [8], Ir_2O_3 [9,10], IrO_2 [8], and IrO_3 [7–9,11–14] was suggested as candidates of gaseous oxides, now it is widely accepted that IrO_3 is the dominant molecule [15,16]. Desorption of gaseous IrO_3 is also observed at oxygen evolution reactions on iridium-based electrodes [17,18]. To prevent the IrO_3 desorption, some researchers have studied iridium-based alloys, such as iridium-rhenium alloys [19] and iridium-aluminum alloys [16]. Despite a number of worthwhile studies, fundamental understanding of the IrO_3 desorption is still absent, which should enhance further material design to reduce the oxidation loss of iridium.

From the theoretical side, first-principles calculations have been performed for surface oxidation of iridium with various surface indices: Ir(100) [20–22], Ir(110) [23,24], and Ir(111) [25,26]. However, all of the previous studies have focused on uniform surface oxidation as thermal equilibria. To obtain insight into the oxidation loss of iridium, it is necessary to trace the fundamental reaction steps including pre-oxidation, precursors, transition states, and of course the final state of IrO_3-desorbed surfaces. In this sense, our understanding is thus far limited to the very beginning of the process of the oxidation loss. It has been identified by the above first-principles studies that the oxygen coverage is low at high temperatures. Thus, a scenario of the IrO_3 desorption from thin passivation films of IrO_2 is less likely. Another problem is that IrO_3 molecules are unstable at room temperature. Thus, there is no experimental data for the free energy of IrO_3. It means that the temperature-dependent chemical potential of IrO_3 must be calculated theoretically by, e.g., density functional theory considering the translational, rotational, and vibrational terms of excitation.

In this study, fundamental reaction steps of Ir oxidation loss are investigated using first-principles calculations. First, we propose a theoretical scheme to identify temperatures, where the oxidation loss occurs. We divide the reaction into three steps: initial oxidation of iridium surfaces, additional oxygen adsorption on a specific Ir site, and the IrO_3 desorption. For each step, free energies for adsorption or desorption are calculated [27]. Next, the scheme is applied to Ir surfaces. We find the close-packed (111) surface is surprisingly active for the IrO_3 desorption for a high-temperature range, where the equilibrium coverage of oxygen is below 0.25 monolayer (ML). We also demonstrate the reaction is more feasible at kinks. The temperature range of the desorption we estimate is consistent with the experimental knowledge that it does not occur below 1373 K [7]. At low temperatures, the IrO_3 desorption itself has high energy barriers. In contrast, the

* Corresponding author.
E-mail addresses: seo.i.ab@m.titech.ac.jp (I. Seo), gohda.y.ab@m.titech.ac.jp (Y. Gohda).

https://doi.org/10.1016/j.commatsci.2020.109897
Received 20 April 2020; Received in revised form 18 June 2020; Accepted 18 June 2020

formation of precursors by oxidation of a specific Ir site becomes difficult at high temperatures. Moreover, the reaction path of the IrO_3 desorption is ascertained in accordance with the nudged elastic band (NEB) method [28,29], where we identify the absence of a transition state.

2. Methodology

Here, we propose a scheme to identify the temperature dependence of the Ir oxidation loss. We first divide the whole reaction into three steps. Then, free energies for adsorption or desorption are calculated considering the entropy of O_2 and IrO_3 molecules.

2.1. Reaction steps

The desorbability of IrO_3 molecules is estimated from three reaction steps. In Step 1, the temperature dependence of initial oxidation state of Ir surfaces is examined. In Step 2, the formation free energy of a precursor, a specific Ir site with three oxygen adatoms, is estimated, which depends on the oxygen precoverage. In Step 3, the desorption free energy of IrO_3 is calculated. A reaction path in the case of the absence of Step 1 (no preoxidation) is depicted in Fig. 1. In the following, the details of each reaction steps are described.

Step 1: We examine oxygen-precovered surfaces up to 1 ML for all of the low-index surfaces, Ir(111), Ir(100), and Ir(110). The most stable adsorption site is identified among three high-symmetry sites for each surface and each coverage. In this step, we evaluate the oxygen-adsorption free energy G_{ads} to identify the temperature-dependent oxygen coverage.

Step 2: For the most stable oxygen-precovered surfaces, oxygen atoms are further adsorbed to form the precursor, a specific Ir site with three oxygen adatoms. We exclude the adsorption of oxygen molecules due to the low oxygen-dissociation energy barrier from the previous study [30]. The number of additional oxygen atoms ΔN_{O} ranges from 0 to 3 in this step. Note that the addition of three oxygen atoms cannot form the precursor in some cases as we discuss later. In this step, we evaluate incremental changes in the oxygen-adsorption free energy ΔG_{ads} from Step 1, as the formation free energy of the precursor.

Step 3: The IrO_3 precursor desorbes from Ir surfaces. The IrO_3-desorption free energy G_{des} is evaluated. Using the NEB method [28,29], the existence of transition states is also examined.

2.2. Thermodynamics approach

Adsorption and desorption free energies are calculated considering molecular excitation [27]. First, the oxygen-adsorption free energy $G_{\mathrm{ads}}(T, p)$ is approximated as

$$G_{\mathrm{ads}}(T, p) \approx E_{\mathrm{Ir-O}} - E_{\mathrm{clean}} - N_{\mathrm{O}}\mu_{\mathrm{O}}(T, p), \tag{1}$$

where $E_{\mathrm{Ir-O}}$ is the total energy of an oxygen-adsorbed surface, E_{clean} is the total energy of a clean Ir surface, N_{O} is the number of adsorbed oxygen atom, and $\mu_{\mathrm{O}}(T, p)$ is the chemical potential of oxygen with the partial pressure p. In this paper, we exploit the chemical potential of O as $\mu_{\mathrm{O}}(T, p) = \frac{1}{2}\mu_{\mathrm{O}_2}(T, p)$.

With the ideal gas approximation, temperature and pressure dependence of the chemical potential $\Delta\mu_i(T, p)$ of a gas molecule i is separated from the total chemical potential $\mu_i(T, p)$ as

$$\mu_i(T, p) = \mu_i^0 + \Delta\mu_i(T, p). \tag{2}$$

The zero-temperature chemical potential μ_i^0 is obtained as the total energy of an isolated molecule from first principles. In the case of O_2, we exploit the JANAF thermochemical table [31] to calculate $\Delta\mu_{\mathrm{O}_2}$. On the other hand, IrO_3 has no experimental thermodynamical data to calculate $\Delta\mu_{\mathrm{IrO}_3}$. Alternatively, we make use of the so-called third-law analysis [32], where thermodynamical considerations for a polyatomic molecule are divided into three terms: the translational, rotational, and vibrational contributions. Thus, $\Delta\mu_i$ is written as $\Delta\mu_i = \Delta\mu_{i,\mathrm{tr}} + \Delta\mu_{i,\mathrm{rot}} + \Delta\mu_{i,\mathrm{vib}}$, where $\Delta\mu_{i,\mathrm{tr}}$, $\Delta\mu_{i,\mathrm{rot}}$, $\Delta\mu_{i,\mathrm{vib}}$ are the translational, rotational, and vibrational contributions to $\Delta\mu_i$, respectively. From statistical mechanics, all of the contributions in $\Delta\mu_i$ are

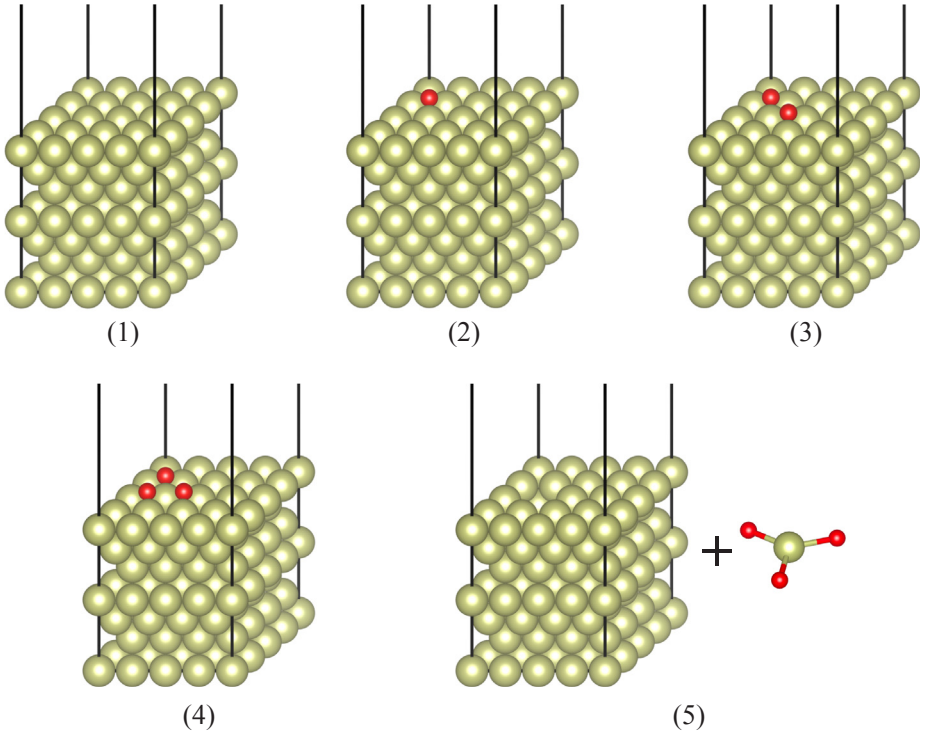

Fig. 1. Whole reaction path for the Ir(111) clean surface in the absence of Step 1. Lime-colored (red) spheres indicate Ir (O) atoms, respectively. Step 2 corresponds to reactions (1) → (2) → (3) → (4), whereas Step 3 is the reaction (4) → (5). (For interpretation of the references to color in this figure legend, the reader is referred to the web version of this article.)

described as

$$\Delta\mu_{i,\mathrm{tr}} = k_\mathrm{B}T\log\left[\frac{p}{k_\mathrm{B}T}\left(\frac{h^2}{2\pi m k_\mathrm{B}T}\right)^{\frac{3}{2}}\right], \tag{3}$$

$$\Delta\mu_{i,\mathrm{rot}} = -k_\mathrm{B}T\log\left[\left(\frac{DT^3}{\sigma^2}\right)^{\frac{1}{2}}\left(\frac{8\pi^{\frac{7}{3}}k_\mathrm{B}}{h^2}\right)^{\frac{3}{2}}\right], \tag{4}$$

$$\Delta\mu_{i,\mathrm{vib}} = k_\mathrm{B}T\sum_{\omega}\log(1-e^{-\hbar\omega/k_\mathrm{B}T}), \tag{5}$$

where k_B, h, $\hbar$, m, D, σ, and ω are the Boltzmann constant, the Planck constant, the reduced Planck constant, the molecular mass, the determinant of the inertia tensor, the symmetry number of the molecule, and the angular frequency of each molecular vibration, respectively. Using the above formulae, $\Delta\mu_{\mathrm{IrO_3}}$ and, thus, $\mu_{\mathrm{IrO_3}}(T, p)$ is obtained on the basis of density functional theory.

Next, the IrO_3-desorption free energy G_des is calculated as

$$G_\mathrm{des}(T, p) \approx E_\mathrm{after} + \mu_{\mathrm{IrO_3}}(T, p) - E_\mathrm{before}, \tag{6}$$

where E_after and E_before are the total energies of a Ir surface before and after the IrO_3 desorption in Step 3.

2.3. Computational details

Our first-principles calculations are based on density functional theory, where the norm-conserving pseudopotentials and pseudoatomic-orbitals are used as implemented in the OpenMX code [33]. The electronic exchange-correlation effects are treated within the generalized gradient approximation (GGA) as the functional proposed by Perdew, Burke, and Ernzerhof (PBE) [34]. As basis sets, s3p2d2 configurations with 7.0-Bohr cutoff radius for Ir and 7.0-Bohr s3p3d2 for O are adopted, where semicore states of Ir 5p are treated as the valence. We use slab models, where, in Step 2 and Step 3, 4 × 4-surface supercells are employed for Ir(100) and Ir(111) surfaces as well as the $2\sqrt{2} \times 2\sqrt{2}$ supercell for Ir(110). To ensure the high accuracy of the calculations, we perform the convergence tests for the cutoff energy and k-grid. With these examinations, 600 Ry of the cutoff energy, and 3 × 3 × 1 k-grid for Step 2 and Step 3 are adopted. Also, from the convergence tests, the number of layers for the Ir slab models are selected as 7 layers for Ir(111), 9 layers for Ir(100), and 13 layers for Ir (110), where 3, 4, and 6 bottom layers of each slab are fixed at the coordinates of fcc Ir, respectively. The convergence criterion for the total energy is chosen as 10^{-6} Hartree, and the criterion for the force on atoms is determined as 10^{-3} Hartree/Bohr for the NEB calculations, 10^{-4} Hartree/Bohr for all the other calculations. We confirmed that the surfaces are always spin-unpolarized, whereas spin degree of freedom is explicitly incorporated for isolated molecules. Spin polarization is also included in NEB calculations. The thickness of the vacuum layer between the slabs is regulated at least 14 Å, and we use 20 Å or more of vacuum layers for NEB calculations in order to guarantee sufficient space for the IrO_3 desorption. Free energies are evaluated using the partial pressure of O_2 as $p_{O_2} = 1$ atm and that of IrO_3 as $p_{\mathrm{IrO_3}} = 10^{-11}$ atm.

3. Results and discussion

First, we discuss the case of the Ir(111) clean surface in the absence of Step 1 for simplicity. In Step 2, ΔG_ads is evaluated, whereas G_des is calculated in Step 3. Note that ΔG_ads is defined as the change in G_ads by additional oxidation attributed to ΔN_O oxygen atoms. Due to the absence of preoxidation, ΔG_ads is identical with G_ads in this case. Fig. 2 shows the free energy profile for the reaction path in the case of the Ir (111) clean surface. The reaction coordinates correspond to the ones in Fig. 1. As is clear from the figure, the energy barrier of the overall

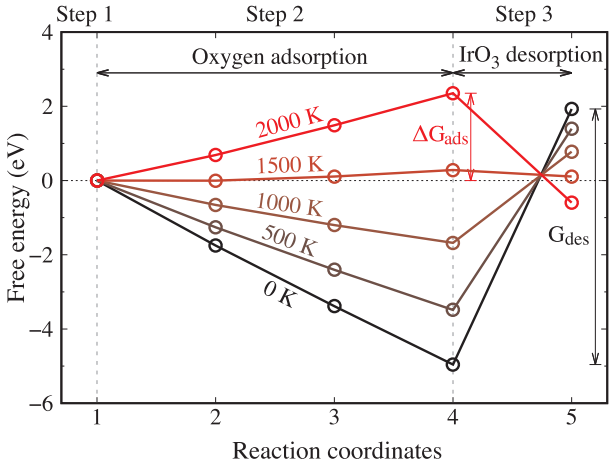

Fig. 2. Free-energy profile for the reaction path in the case of the Ir(111) clean surface. The reaction coordinates correspond to the ones in Fig. 1. The red vertical arrow indicates ΔG_ads for $T = 2000$ K, while the black vertical arrow corresponds to G_des for $T = 0$. (For interpretation of the references to color in this figure legend, the reader is referred to the web version of this article.)

reaction is attributed to Step 3 at low temperatures. For example, G_des is obviously dominant for $T = 0$. On the contrary, Step 2 prevents the IrO_3 desorption at very high temperatures (see, e.g., ΔG_ads for $T = 2000$ K): The desorption never occurs without O adsorption.

Next, whole reaction paths considering Step 1 are examined for the (111), (100), and (110) surfaces as in Fig. 3. Surface preoxidation is examined as Step 1. In every oxygen coverage, the fcc–hollow site for Ir (111) and the bridge site for Ir(100) and Ir(110) are the most stable, which is in good agreement with previous studies [20–26]. Oxygen-adsorption free energy G_ads determines the most stable coverage as a function of temperature. It is generally seen that the oxygen coverage decreases as the temperature increases.

The precursor formation is studied in Step 2. Here, $\Delta G_\mathrm{ads} = 0$ corresponds to the case of $\Delta N_\mathrm{O} = 0$, where the precursor is already formed by the preoxidation in Step 1. In contrast, it is obvious that the clean surface requires the condition of $\Delta N_\mathrm{O} = 3$. Additional oxygen atoms are adsorbed on the same sites as the precovered oxygen atoms shown in Fig. 4 with the exception in Ir(110): adsorption on the site 3 in Fig. 4(c) occurs only for high-coverage cases preventing the formation of the precursor. In the case of Ir(111), ΔG_ads becomes remarkably high for $T > 1600$ K, where the possibility of the precursor formation is completely excluded for the clean surface. In contrast, ΔG_ads can be low at some temperature ranges including the one around 1500 K. It is noted that ΔG_ads should be non-negative, because Step 2 is out of equilibrium starting from a surface-phase equilibrium. The discrepancy seen for, e.g., $T \approx 800$ K means that the coverage in equilibrium is not 0.5 ML, but between 0.5 and 0.75 ML. Here, we will not proceed further for the two temperature ranges of this discrepancy, because they are in any case irrelevant considering Step 3 as discussed below. As for the cases of Ir(100) and Ir(110), ΔG_ads is in principle very high. Note that ΔG_ads is not obtained for some cases, where the precursor is not energetically stable. Thus, Ir(100) and Ir(110) are not suitable for the precursor formation excluding the possibility of the IrO_3 desorption.

The IrO_3 desorption is examined by using G_des in Step 3. As is clear from Fig. 3, G_des in the case of Ir(111) is remarkably high for $T < 1300$ K, where the IrO_3 desorption is not expected. Summarizing the above results for ΔG_ads and G_des, the possibility for the IrO_3 desorption from the low-index surfaces can be excluded except for the case of the Ir(111) surface at the temperature range of $1300 < T < 1600$ K. Since it is difficult to examine all possible precoverages in Step 1, our estimation of the temperature range has ambiguity. However, it is considered to be safe to say that the IrO_3 desorption is possible enough for

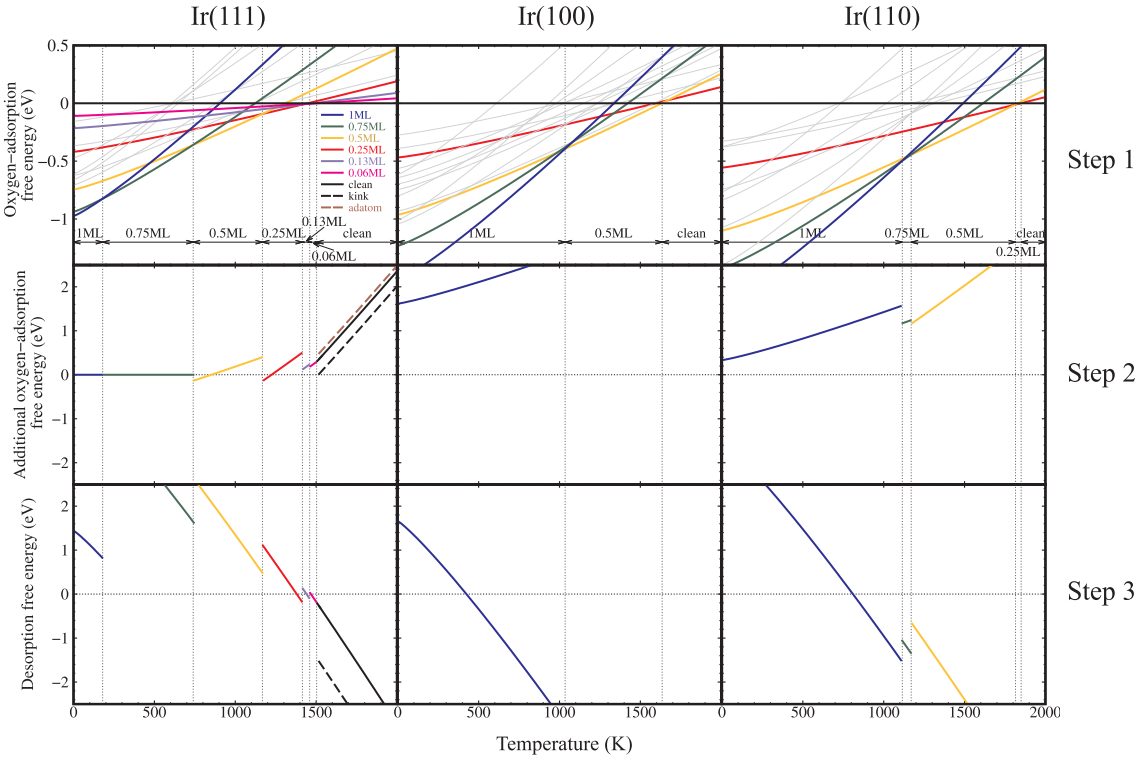

Fig. 3. Step 1: Oxygen-adsorption free energy G_{ads} per 1×1 supercell. Step 2: Additional oxygen-adsorption free energy ΔG_{ads} for the most stable surfaces identified in Step 1. Step 3: IrO_3-desorption free energy G_{des}. The free energy for each coverage with the most stable configuration is highlighted with thick solid lines. Note that the desorption free energy of adatom, which is −3.9 eV at 1500 K, is not displayed. (For interpretation of the references to color in this figure legend, the reader is referred to the web version of this article.)

$1400 < T < 1500$ K from the close-packed Ir(111) surface with the oxygen precoverage of less than 0.25 ML. The present result is consistent with experimental studies reporting desorption of Ir at around 1373 K or higher [7].

In general, surfaces with kinks and steps are considered as more reactive than the terrace of a surface [35]. Thus, we examine the effect of kinks at the clean (111) surface using a vicinal (11 7 5) surface. Here, we employed the $\sqrt{2} \times \sqrt{2}$ supercell of the (11 7 5) surface to avoid fictitious interaction between neighboring precursors. It is clear from Fig. 3 that both ΔG_{ads} and G_{des} decreases compared with those of the (111) terrace. Thus, it is expected that the temperature range of the IrO_3 desorption increases from $1400 < T < 1500$ K. In particular, the upper bound should increase by approximately 100 K. In contrast, the lower limit is expected to be unchanged, because ΔG_{ads} is high enough for the coverage of 0.25 ML. The adatom on (111) terrace is also inspected. The result shows considerable decrease of G_{des}, nevertheless, ΔG_{ads} is increased 0.12 eV oppositely. Therefore, it should not affect to the temperature range.

As we already mentioned, the most significant factor to prevent the IrO_3 desorption from Ir(100) or Ir(110) is high oxygen-adsorption free energies. The reason for the difficulty in the precursor formation can be explained using atomic arrangements of precursors shown in Fig. 4. The precursor at the Ir(111) surface has an adequate O–O distance contributing to the stability of the precursor. In contrast, the shortest O–O distance for the case of Ir(100) is too short making the precursor unstable. As for the case of Ir(110), the third adatom has high energy cost to adsorb, and, thus, the precursor is less stable, too. These are the reasons that ΔG_{ads} is high for Ir(100) and Ir(110).

As is clear from Figs. 1 and 2, only the initial and final states have been monitored thus far for Step 3. To obtain further insight into the reaction path in Step 3, we examined the possibility of a transition state using the NEB method for various Ir surfaces. For all of the cases examined, no transition state is seen as shown in Fig. 5. The absence of transition states guarantees the validity of the discussion in the present study using G_{des} as the energy barrier. It should be noted that the energy profile is not monotonous for some cases. For example, for the Ir(111) clean surface, the IrO_3 desorption occurs with the following order: i) large displacement of one O atom from the surface maintaining one Ir–O bond with a large energy increase; ii) subsequent displacement of Ir atom with three Ir–O bonds from the surface with a modest energy

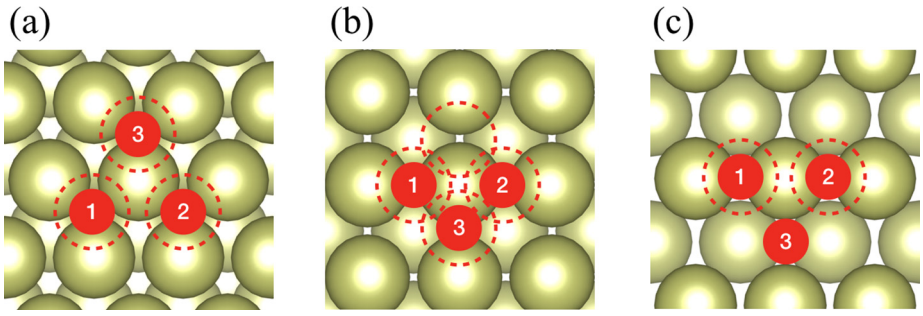

Fig. 4. The most stable oxygen-adsorption sites of (a) Ir(111), (b) Ir(100), (c) Ir(110) surfaces to form the IrO_3 precursor. Red dotted circles are the most stable oxygen-adsorption sites in every oxygen coverage, and filled red circles are adsorbed oxygen atoms to form the precursor on the surface. (For interpretation of the references to color in this figure legend, the reader is referred to the web version of this article.)

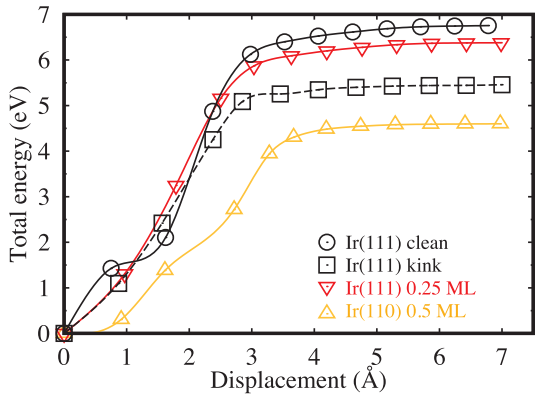

Fig. 5. Energy profile of the reaction path within Step 3 for the clean Ir(111) surface, the clean Ir(111) surface with kinks, the Ir(111) surface with the 0.25-ML oxygen coverage, and the Ir(110) surface with the 0.5-ML coverage. The horizontal axis represents the displacement of the Ir atom within IrO_3 in the direction perpendicular to the surface, which is referenced to the initial state. (For interpretation of the references to color in this figure legend, the reader is referred to the web version of this article.)

increase; iii) displacement of two O atoms finalizing the IrO_3 desorption with a large energy increase.

4. Conclusions

We have investigated about the IrO_3 desorption from the iridium low-index surfaces by first-principles calculations. Using the theoretical scheme, where the reaction is divided into three reaction steps, adsorption and desorption free energies were evaluated. The IrO_3 desorption occurs from the close-packed Ir(111) surface for the temperature range of approximately $1400 < T < 1500$ K, where the equilibrium coverage of oxygen is below 0.25 ML. The temperature range is expected to become wider with the upper bound of 1600 K by considering the effect of kinks. The lower limit of the desorption temperature is consistent with experiments reporting it as 1373 K. From less close-packed (100) and (110) surfaces, the desorption is not expected. The usefulness of the desorption free energy was supported by the NEB method confirming the absence of transition barriers. Since our scheme is applicable to surfaces other than Ir, fundamental understanding of desorption processes from various material surfaces will be deepened, which should enhance material design of alloys to prevent undesired desorption loss.

Declaration of Competing Interest

The authors declare that they have no known competing financial interests or personal relationships that could have appeared to influence the work reported in this paper.

CRediT authorship contribution statement

Insung Seo: Methodology, Formal analysis, Investigation, Visualization, Writing - original draft. **Shunsuke Yokota:** Conceptualization, Resources. **Yousuke Imai:** Conceptualization, Resources. **Yoshihiro Gohda:** Conceptualization, Funding acquisition, Methodology, Validation, Resources, Supervision, Project administration, Writing - review & editing.

Acknowledgements

This work was supported in part by JSPS KAKENHI Grant No. 17K04978. We are grateful to Tomonori Tanaka and Asako Terasawa for fruitful discussions. The calculations were partly carried out by using supercomputers at ISSP, The University of Tokyo, and TSUBAME, Tokyo Institute of Technology as well as the K computer, RIKEN (Project Nos. hp180206 and hp190169).

Appendix A. The IrO_3 molecule

Here, the structure and the stability of the IrO_3 molecule are discussed. We first carried out calculations of an isolated IrO_3 molecule. Heretofore, the IrO_3 molecule has been expected as the trigonal planar structure consisting of the angle of 120° with the three Ir–O terminations [15,36]. Our results show that IrO_3 is planar, but the threefold symmetry is broken, as the bond angles are obtained as 113.44°, 113.44°, and 133.12°. In addition, the Ir–O distances are 1.73 Å, 1.73 Å, and 1.78 Å. To confirm the validity of the results obtained by GGA-PBE, we also carried out calculations with a non-*ab initio* exchange-correlation functional, which is nevertheless very typical for molecules, the B3LYP functional [37,38], by using the VASP code [39–42]. The B3LYP functional provides very similar results: 113.95°, 113.95°, and 132.10° for the bond angles as well as 1.70 Å, 1.70 Å, and 1.76 Å for the bond lengths. Vibrational frequencies $\hbar\omega$ are calculated by the direct method: The B3LYP functional provides 26.70, 29.76, 35.71, 105.74, 112.13, and 123.99 meV, whereas the GGA-PBE functional results in the values of 18.14, 25.40, 34.32, 108.85, 113.23, and 118.86 meV. Since the vibrational frequency comes from a second-order derivative of the total energy, the functional dependence becomes rather large. Considering the fact that the B3LYP functional is particularly optimized for isolated molecules, we used the B3LYP frequencies to calculate the chemical potential of the IrO_3 molecule.

As IrO_3, IrO_2, Ir_2O_3 [43], and IrO have been suggested as candidates of the iridium gaseous oxides, we compared the energetic stability of these molecules. To evaluate the stability of iridium gaseous oxides, we employ the formation energy. Considering fcc Ir and O_2 as thermal reservoirs, the formation energy, E_{form} is established as

$$E_{\mathrm{form}} = E_{\mathrm{molecule}} - N_{\mathrm{Ir}}\mu^0_{\mathrm{Ir}} - N_{\mathrm{O}}\mu^0_{\mathrm{O}}, \tag{7}$$

where E_{molecule} is the energy of a single molecule, and N_{Ir} is the number of Ir atoms, and μ^0_{Ir} is the Ir zero-temperature chemical potential that is the total energy of fcc Ir. By using GGA-PBE, E_{molecule} for IrO_3, IrO_2, Ir_2O_3, and IrO becomes 0.27 eV, 1.90 eV, 3.10 eV, and 5.12 eV, respectively. The positive values of E_{molecule} coincide with the fact that these molecules are not observed at room temperature. Nevertheless, it should be reasonable to consider that the IrO_3 molecule is responsible for the oxidation loss of Ir as have been reported in previous studies [15,16], because IrO_3 is prominently most stable among these molecules. In addition, other molecules are not to be expected to emerge within the reaction path of the IrO_3 desorption considering the high formation energies.

References

[1] J.G. McCarty, M. Gusman, D.M. Lowe, D.L. Hildenbrand, K.N. Lau, Stability of supported metal and supported metal oxide combustion catalysts, Catal. Today 47 (1999) 5–17, https://doi.org/10.1016/S0920-5861(98)00279-X.
[2] E.A. Gulbransen, K.F. Andrew, F.A. Brassart, Oxidation of Molybdenum 550 to 1700C, J. Electrochem. Soc. 110 (1963) 952–959, https://doi.org/10.1149/1.2425918.
[3] F.D. Richardson, Iridium as a high temperature material, Platin. Met. Rev. 2 (1958)

83–85.
[4] L.B. Hunt, A history of iridium, Platin. Met. Rev. 31 (1987) 32–41.
[5] H. Osamura, N. Abe, Development of New Iridium Alloy for Spark Plug Electrodes, SAE Tech. Pap (1999) 1999-01-0796, doi: 10.4271/1999-01-0796.
[6] W. Crookes, On the use of iridium crucibles in chemical operations, Porc. R. Soc. Lond. Series A 80 (1908) 535–536.
[7] H. Jehn, R. Völker, M.I. Ismail, Iridium losses during oxidation, Platin. Met. Rev. 22 (1978) 92–97.
[8] J.H. Norman, J.G. Staley, W.E. Bell, Mass-spectrometric study of gaseous oxides of iridium, J. Chem. Phys. 42 (1965) 1123–1124, https://doi.org/10.1063/1.1696054.
[9] M.S. Chandrasekharaiah, M.D. Karkhanavala, S.N. Tripathi, The pressure of iridium oxides over iridium at high temperatures in 1 atm of dry oxygen, J. Less-Common Met. 80 (1981) 9–17, https://doi.org/10.1016/0022-5088(81)90162-4.
[10] S.N. Tripathi, M.S. Chandrasekharaiah, A new gaseous iridium oxide, Ir2O3, High Temp. Sci. 17 (1984) 365–369, https://doi.org/10.1007/978-1-4612-5180-4_20.
[11] E.H.P. Cordfunke, G. Meyer, The system iridium - oxygen I. Measurements on the volatile oxide of iridium, Recl. Trav. Chim. Pays-Bas 81 (1962) 495–504, https://doi.org/10.1002/recl.19620810608.
[12] W.E. Bell, M. Tagami, Study of gaseous oxides, chloride, and oxychloride of iridium, J. Phys. Chem. 70 (1966) 640–646, https://doi.org/10.1021/j100875a007.
[13] R.T. Wimber, H.G. Kraus, Oxidation of iridium, Metall. Trans. 5 (1974) 1565–1571, https://doi.org/10.1007/BF02646327.
[14] E.S. Ramakrishnan, M.S. Chandrasekharaiah, The activity of iridium in iridium-platinum alloys by a transpiration method, J. Less-Common Met. 37 (1974) 269–280, https://doi.org/10.1016/0022-5088(74)90042-3.
[15] J.H. Carpenter, Equilibrium reaction of iridium and oxygen at high temperatures, J. Less-Common Met. 152 (1989) 35–45, https://doi.org/10.1016/0022-5088(89)90069-6.
[16] H. Hosoda, S. Miyazaki, S. Hanada, Potential of IrAl base alloys as ultrahigh-temperature smart coatings, Intermetallics 8 (2000) 1081–1090, https://doi.org/10.1016/S0966-9795(00)00074-1.
[17] O. Kasian, J.P. Grote, S. Geiger, S. Cherevko, K.J.J. Mayrhofer, The common intermediates of oxygen evolution and dissolution reactions during water electrolysis on iridium, Angew. Chem. Int. Ed. 57 (2018) 2488–2491, https://doi.org/10.1002/anie.201709652.
[18] C. Spöri, J.T.H. Kwan, A. Bonakdarpour, D.P. Wilkinson, P. Strasser, The stability challenges of oxygen evolving catalysts: towards a common fundamental understanding and mitigation of catalyst degradation, Angew. Chem. Int. Ed. 56 (2017) 5994–6021, https://doi.org/10.1002/anie.201608601.
[19] B. Reed, High temperature oxidation behavior of iridium-rhenium alloys, AIAA Meeting Paper (1994) 94–2893, https://doi.org/10.2514/6.1994-2893.
[20] I.A. Erikat, B.A. Hamad, J.M. Khalifeh, Adsorption of O and CO on Ir(100) from first principles, Eur. Phys. J. B 67 (2009) 35–41, https://doi.org/10.1140/epjb/e2008-00471-7.
[21] C. He, H. Wang, L. Huai, J. Liu, Mechanism of ammonia decomposition and oxidation on Ir(100): a first-principles study, J. Phys. Chem. C 116 (2012) 24035–24045, https://doi.org/10.1021/jp305399g.
[22] P. Ferstl, T. Schmitt, M.A. Schneider, L. Hammer, A. Michl, S. Müller, Structure and ordering of oxygen on unreconstructed Ir(100), Phys. Rev. B 93 (2016) 235406, , https://doi.org/10.1103/PhysRevB.93.235406.
[23] J.L. Taylor, D.E. Ibbotson, W.H. Weinberg, The chemisorption of oxygen on the (110) surface of iridium, Surf. Sci. 79 (1979) 349–384, https://doi.org/10.1016/0039-6028(79)90295-4.
[24] P. Kaghazchi, T. Jacob, First-principles studies on clean and oxygen-adsorbed Ir (110) surfaces, Phys. Rev. B 76 (2007) 245425, , https://doi.org/10.1103/PhysRevB.76.245425.
[25] W.P. Krekelberg, J. Greeley, M. Mavrikakis, Atomic and molecular adsorption on Ir (111), J. Phys. Chem. B 108 (2004) 987–994, https://doi.org/10.1021/jp035786c.
[26] H. Zhang, A. Soon, B. Delley, C. Stampfl, Stability, structure, and electronic properties of chemisorbed oxygen and thin surface oxides on Ir(111), Phys. Rev. B 78 (2008) 045436, , https://doi.org/10.1103/PhysRevB.78.045436.
[27] K. Reuter, M. Scheffler, Composition, structure, and stability of RuO2(110) as a function of oxygen pressure, Phys. Rev. B 65 (2001) 035406, , https://doi.org/10.1103/PhysRevB.65.035406.
[28] H. Jónsson, G. Mills, K.W. Jacobsen, Nudged elastic band method for finding minimum energy paths of transitions, in: B.J. Berne, G. Ciccotti, D.F. Coker, Classical and Quantum Dynamics in Condensed Phase Simulations, World Scientific, Singapore, 1998, Chapter 16, pp. 385–404.
[29] G. Henkelman, H. Jónsson, Improved tangent estimate in the nudged elastic band method for finding minimum energy paths and saddle points, J. Chem. Phys 113 (2000) 9978–9985, https://doi.org/10.1063/1.1323224.
[30] Y. Xu, M. Mavrikakis, Adsorption and dissociation of O2 on Ir(111), J. Chem. Phys. 116 (2002) 10846, https://doi.org/10.1063/1.1479716.
[31] M.W.J. Chase, NIST-JANAF Thermochemical Tables, fourth ed., American Institute of Physics, New York, 1998.
[32] G.N. Lewis, M. Randall, Thermodynamic properties of ideal gases calculated from spectroscopic and other molecular data, in: K.S. Pitzer, L. Brewer (Eds.), Thermodynamics, McGraw-Hill, New York, 1961, pp. 419–448.
[33] T. Ozaki, Variationally optimized atomic orbitals for large-scale electronic structures, Phys. Rev. B 67 (2003) 155108, , https://doi.org/10.1103/PhysRevB.67.155108.
[34] J.P. Perdew, K. Burke, M. Ernzerhof, Generalized gradient approximation made simple, Phys. Rev. Lett. 77 (1996) 3865, https://doi.org/10.1103/PhysRevLett.77.3865.
[35] A. Groß, Theoretical Surface Science, second ed., Springer, Berlin Heidelberg, 2009, pp. 146–152.
[36] A. Citra, L. Andrews, Reactions of laser-ablated iridium atoms with O^2. Infrared spectra and DFT calculations for iridium dioxide and Peroxo Iridium(VI) dioxide in solid argon, J. Phys. Chem. A 103 (1999) 4182–4190, https://doi.org/10.1021/jp990388o.
[37] A.D. Becke, A new mixing of Hartree-Fock and local density-functional theories, J. Chem. Phys. 98 (1993) 1372–1377, https://doi.org/10.1063/1.464304.
[38] A.D. Becke, Density-functional thermochemistry. III. The role of exact exchange, J. Chem. Phys. 98 (1993) 5648–5652, https://doi.org/10.1063/1.464913.
[39] G. Kresse, J. Furthmüller, Efficient iterative schemes for ab initio total-energy calculations using a plane-wave basis set, Phys. Rev. B (1996) 11169, https://doi.org/10.1103/PhysRevB.54.11169.
[40] G. Kresse, J. Furthmüller, Efficiency of ab-initio total energy calculations for metals and semiconductors using a plane-wave basis set, Comput. Mater. Sci. 6 (1996) 15–50, https://doi.org/10.1016/0927-0256(96)00008-0.
[41] P.E. Blöchl, Projector augmented-wave method, Phys. Rev. B 50 (1994) 17953, https://doi.org/10.1103/PhysRevB.50.17953.
[42] G. Kresse, D. Joubert, From ultrasoft pseudopotentials to the projector augmented-wave method, Phys. Rev. B 59 (1999) 1758, https://doi.org/10.1103/PhysRevB.59.1758.
[43] X. Zhou, J. Yang, C. Li, Theoretical study of structure, stability, and the hydrolysis reactions of small iridium oxide nanoclusters, J. Phys. Chem. A 116 (2012) 9985–9995, https://doi.org/10.1021/jp3064068.